TOC Graphics

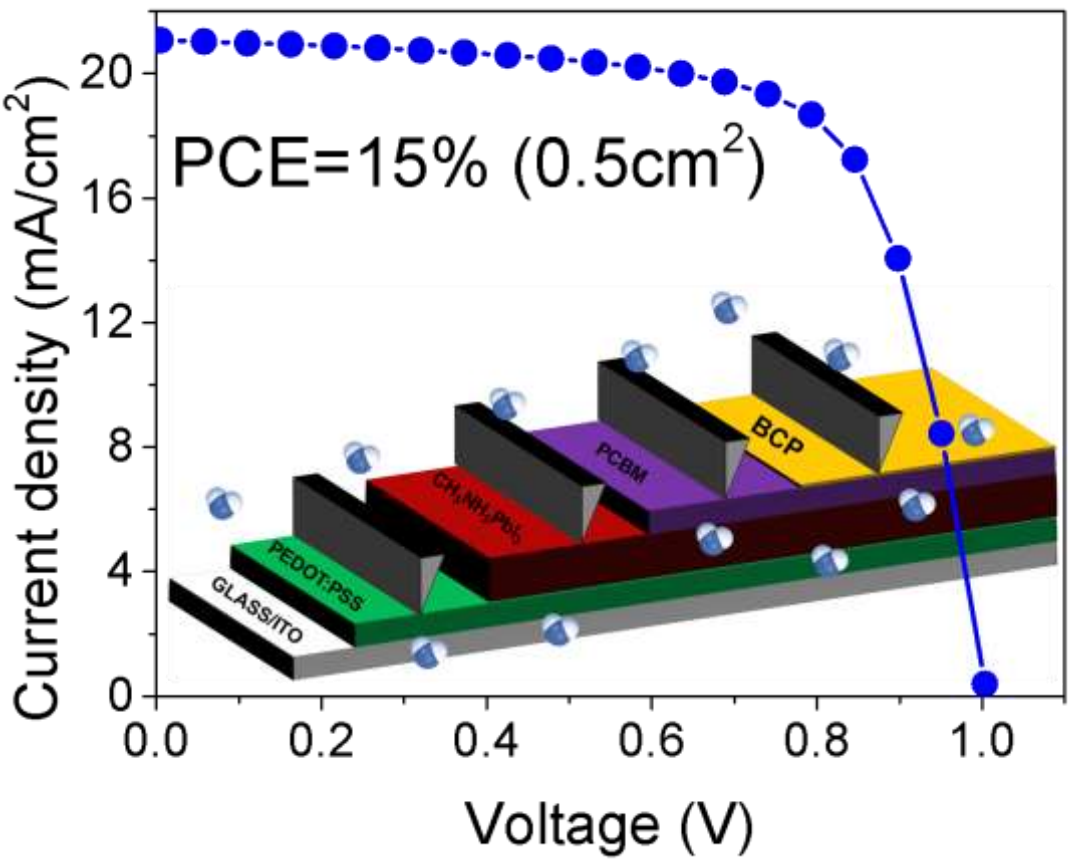

Fully air-printed perovskite solar cell incorporating a nanometer-thick blade coated bathocuproine (BCP) buffer layer (ITO/PEDOT:PSS/$CH_3NH_3PbI_3$/PCBM/BCP/Ag). The BCP layer was blade coated for the first time being also printed in humid air (RH

<50%), and PSCs delivered a PCE of 14.9% proving its compatibility with S2S and R2R manufacturing.

Efficient Fully Blade-coated Perovskite Solar Cells in Air with Nanometer-thick Bathocuproine Buffer Layer

Sergio Castro-Hermosa[a,b,c,*,+], Luana Wouk [a], Izabela Silva Bicalho[a], Luiza de Queiroz Corrêa[a], Bas de Jong[d,e], Luciò Cinà[d], Thomas M Brown[b], Diego Bagnis[a,+]

[a] CSEM Brasil, Avenida José Cândido da Silveira, 2000, 31035-536, Belo Horizonte, Brazil

[b] CHOSE (Centre for Hybrid and Organic Solar Energy), Department of Electronic Engineering, University of Rome Tor Vergata, Via del Politecnico 1, 00133 Rome, Italy

[c] Hydro Engineering and Agricultural Development Research Group (GHIDA), Faculty of Engineering, Universidad Surcolombiana, Avenida Pastrana Borrero-Carrera 1, 410001 Neiva, Colombia

[d] Cicci Research srl, via Giordania 227, Grosseto 58100, Italy

[e] Department of Biotechnology, Chemistry and Pharmacy, University of Siena, Via A. Moro 2, Siena 53100, Italy

Abstract: Fully printed perovskite solar cells (PSCs) were fabricated in air with all constituent layers, except for electrodes, deposited by the blade coating technique. The PSCs incorporated, for the first time, a nanometer-thick printed Bathocuproine (BCP) hole blocking buffer using blade coating technique and deposited at relative humidity up to 50%. The PSCs with a p-i-n architecture (Glass/Indium tin oxide(ITO)/poly(3,4-ethylenedioxythiophene) polystyrene sulfonate (PEDOT:PSS)/$CH_3NH_3PbI_3$ /[6,6]-

* Lead author: sergio.castro@csembrasil.com.br
+ Corresponding authors: sergio.castro@csembrasil.com.br, diego.bagnis@csembrasil.com.br

phenyl-C_{61}-butyric acid methyl ester (PCBM)/BCP/Ag) delivered a maximum power conversion efficiency (PCE) of 14.9% on an active area of 0.5 cm^2 when measured under standard test conditions (STC). The PSCs with a blade coated BCP delivered performance of 10% and 63% higher (in relative terms) than those incorporating a spin coated BCP or without any BCP film, respectively. The atomic force microscopies (AFM) showed that blade coated films were more homogeneous and acted also as a surface planarizer leading to a reduction of roughness which improved BCP/Ag interface reducing charge recombination. The demonstration of 15% efficient devices with all constituent layers, including nanometer-thick BCP (~10 nm), deposited by blade coating in air, demonstrates a route for industrialization of this technology.

Keywords: Perovskite, buffer, bathocuproine (BCP), blade coating, printed electronics.

INTRODUCTION

Perovskite solar cells (PSCs) have achieved remarkable power conversion efficiencies (PCE) of up to 25.2%[1]; however, these efficiencies have been reached at the laboratory scale with small-area devices (0.1 cm^2) fabricated inside high purity environments (i.e nitrogen glovebox) by highly controllable spin coating technique[2], and incorporating interlayers and electrodes that are typically thermally evaporated. Nevertheless, to industrialize the PSCs, both perovskite film and interlayers must be compatible with low-cost large-scale sheet-to-sheet (S2S) or roll-to-roll (R2R) process [3], [4]; therefore, PSCs should be fabricated using printing compatible techniques such as blade and slot-die coating[5]. Blade coating has been widely used in PSCs reaching efficiencies up to 18.6%[6] when a perovskite active layer was deposited by blade coating (in air) and the other constituent layers by either spin (inside glovebox) or spray coating

(in air), and 19.6% [8] for an all blade coated PSC. Similarly, R2R slot-die deposition[7]–[9] of PSCs delivered impressive PCEs of 17%[8] and a maximum PCE of 18% with S2S slot-die deposition[9] when the hole transporting layers were deposited via spin coating. However, these efficiencies have being reporting for PSC with n-i-p structure which incorporated thin layers above 30 nm thick. The most challenging issue in both blade and slot-die deposition is the fast removal of solvent (i.e dimethyl formamide – DMF) while preventing methylammonium (CH_3NH_3) evaporation, to avoid the presence of large grain boundaries[10] where usually the PbI_2 may remain[11]. This issue has been solved by replacing the DMF with high boing solvents such as dimethyl sulfoxide (DMSO) or γ-Butyrolactone (GBL)[12], [13], or replacing the perovskite precursors including the commonly used PbI_2. PbI_2 has been replaced with lead acetate ($Pb(C_2H_3O_2)_2$) or lead chloride ($PbCl_2$) obtaining very reproducible pinhole free films[14]–[19]. Lead acetate based PSCs can be fabricated even in high humidity environment representing and advantage for fabrication and up-scaling[20]. Moreover, the presence of chlorine improves the growth of perovskite by increasing the crystal growth rate and reducing the annealing time[6]. The morphology of perovskite has been also modified and controlled by the drying of wet films by gas quenching [21]–[23]. Perovskite films deposited by blade or slot-die without gas quenching presented high density of pinholes induced for the vertical/columnar growth of crystals resulting in a very low absorbance; however, when a temperature gradient was created by a flow of hot dry air, the growth of perovskite was horizontal leading to compact and smooth films[22]. Similar results were noted when perovskite was dried with nitrogen[21]. Thus, gas quenching/drying secured very smooth pinhole-free perovskite films which are optimal for solar cell fabrication since low roughness at the surface results in low charge recombination enhancing the PCE of PSC[24]–[26]. Once the perovskite deposition is optimized using large scale techniques,

the deposition of nanometer-thick interlayer films becomes the main issue to be resolved since these interlayers reduce charge recombination but they must be compact and nanometer-thick <10 nm[27]–[30]. Generally, the interlayers are placed between the electron transporting layer (ETL) and either the perovskite film or metal electrode (gold, silver or copper depending the implemented solar cell architecture, i.e n-i-p or p-i-n respectively). Films including MgO[29] or Al_2O_3[30], or bathocuproine (BCP) film have been successfully implemented as interlayer for PSCs. PSCs incorporating BCP by spin coating or thermal evaporation have reach performances up to 20% and 22% respectively. Huang group has shown high PCE (~22% in an active area of 0.1 cm^2 [31], [32]) when both ETL and BCP were thermally evaporated. However; either spin coated in an inert atmosphere (i.e N_2 or Ar glovebox [33]–[36]) or thermal-evaporated[37], [38] in vacuum are incompatible processes with R2R manufacturing. Therefore, we present an inverted PSC with all constituent layers, except for electrodes, deposited by blade coating in air at 35-50% relative humidity (RH). The fully printed PSCs possess a p-i-n architecture, i.e. Glass/Indium tin oxide(ITO)/poly(3,4-ethylenedioxythiophene) polystyrene sulfonate (PEDOT:PSS)/$CH_3NH_3PbI_3$ /[6,6]-phenyl-C_{61}-butyric acid methyl ester (PCBM)/BCP/Ag, incorporating a nanometer-thick blade coated bathocuproine buffer which acts as hole blocking layer(HBL), to reduce the charge accumulation and recombination at the PCBM/Ag interface[28]. The BCP layer was blade coated for the first time being also printed in air atmosphere. Fully printed PSCs delivered a maximum PCE of 14.9% proving its compatibility with S2S and R2R manufacturing.

1. EXPERIMENTAL SECTION

1.1. Materials:

All materials were purchased from commercial suppliers and used without further purification. PEDOT:PSS (Clevios P VP AI 4083) was obtained from Heraeus. Perovskite lead sources such as lead (II) acetate trihydrate ($Pb(C_2H_3O_2)_2.3H_2O$, 99.999%) and lead (II) chloride ($PbCl_2$, 99.999%), and anhydrous solvents including N,N-dimethylformamide (DMF, 99.8%), chlorobenzene (CB, 99.8%) and 2-propanol (IPA, 99.5%) were purchased from Sigma-Aldrich. Methylammonium iodide (MAI, CH_3NH_3I) was purchased from Great Cell Solar Materials. The PCBM (99.8%) was purchased from Nano-C while bathocuproine ($C_{26}H_{20}N_2$ >98%) was purchased from TCI Chemicals.

1.2. Perovskite solar cell fabrication process:

All constituent layers of PSCs including the PEDOT:PSS hole transport layer (HTL), methylammonium lead iodide perovskite absorber ($CH_3NH_3PbI_3$), PCBM electron transport layers (ETL), and the BCP hole blocking buffer were fabricated in air at RH range between 35-50%, and using an Erichsen 510 blade coater. The BCP hole blocking buffer was also deposited via spin coating acting as a reference for the blade coating optimization. All cells had a p-i-n planar structure with Glass/ITO/PEDOT:PSS/$CH_3NH_3PbI_3$/PCBM/BCP/Ag architecture. First, the 50x50 mm^2 pre-patterned Glass/ITO substrates (10 $\Omega.sq^{-1}$, Thin Film Devices Inc.) were sequentially cleaned in ultrasonic bath in soapy water, water, acetone and isopropanol for 5 min each and then rapidly dried with nitrogen followed by an UV-O_3 cleaning (NovaScan PSD 4) for 15 min. After substrate cleaning, the PEDOT:PSS (1:3 in isopropanol) film was immediately bladed coated using a gap of 200 µm and speed of 10

mm s^{-1}; the resulting film was annealed at 150°C for 10 min. For perovskite film deposition, the blade coater was modified adding a nitrogen blower developed by CSEM Brasil only when RH was lower than 40%. Therefore, perovskite film was coated with a gap of 100 µm and speed of 10 mm s^{-1} at 43°C, and the resulting wet film was sequentially dried with a nitrogen flow. Then, the sample was transferred to a hot plate for further annealing at 100°C for 30 min. Perovskite ink was compound of $Pb(C_2H_3O_2)_2$, $PbCl_2$ and CH_3NH_3I with a molar ratio of 0.8:0.2:2.9 in DMF. The PCBM powder was dissolved in chlorobenzene with a final concertation of 20mg/mL and deposited with a speed of 10 mm s^{-1} and a gap of 125 µm. Finally, the BCP was mixed with isopropanol in a concentration of 0.5 mg/mL and left in stirring overnight at room temperature. The BCP was deposited either by spin coating or blade coating. Spin coated BCP (4000 rpm for 60s) was used as reference cell, and the blade coated BCP was deposited with a gap of 100 µm at different speeds. All the depositions were carried out in air atmosphere. Finally, the substrates were transferred to a metal evaporator for the deposition of silver back electrode. The evaporation was carried at a pressure of $3x10^{-6}$ mbar and using a shadow mask to define eight cells with an active area of 0.5 cm^2 each.

1.3. Characterization of films:

The XRD spectra were obtained with Cu-Kalfa (λ = 1.54060 Å) radiation source from Shimadzu XRD 7000. The source was operated at 40 kV and 30 mA. The incident angle was fixed at 3° to avoid the interaction with the substrate. The scanning electron microscopy (SEM) images were acquired using a Quanta FEG 3D FEI. The samples were analyzed with accelerating voltage of 5 kV reducing the damages caused by the electron beam. Photoluminescence (PL) and Raman spectroscopy were performed with a confocal Witec Alpha 300 system with a 15 mW and 438 nm excitation source.

1.4. Characterization of PSCs:

The current density-voltage (J-V) curves were measured using a Keithley 2400 Source Measure Unit integrated to a Solar Simulator (Wacom WXS-156S-10) under the standard test conditions: AM 1.5G, 100 $mW.cm^{-2}$ (1 sun equivalent) at room temperature. A certified silicon reference cell (20x20 mm^2) provided by PV Measurements was used to calibrate the intensity of the light source. The voltage sweep was applied from –0.1 to 1.2V at a rate of 100 mVs^{-1}. All samples were kept under constant nitrogen flow during the measurements to prevent degradation. A Bruker Dektak XT profilometer with a 2 μm diameter tip was used for thickness measuring of the deposited films. Transient photovoltage (TPV), transient photocurrent (TPV), electroluminescence (EL) and external quantum efficiency (EQE) tests were performed with an all in one platform (ARKEO - Cicci Research) composed by multichannel 4-wire source meters, 100MS/s digitizer and Arbitrary function generators. EQE is based on a 300 Watts Xenon lamp and double grating (300 to 1400 nm). A correct integration of the incident monochromatic light was made comparing the photo-response of a Si UV-enhanced NIST calibrated photodetector. EL spectra were collected with a 10mm of diameter aspheric lens close to the substrate and recorded by a CCD based spectrometer. Integration time and number of averaging is maintained the same to compare the results. In TPV test a high-speed LED based system (5000 Kelvin) is used to create small perturbation optical signals tuned to maintain voltage deflection within 50 mV. Steady state light was increased by 0.1 to 2 sun equivalent.

2. RESULTS AND DISCUSSION

PSCs with Glass/ITO/PEDOT:PSS/$CH_3NH_3PbI_3$/PCBM/BCP/Ag architecture were successfully fabricated with printing of all the layers, except the two electrodes, in air at 35-50% RH. PEDOT:PSS and PCBM were deposited via standard blade-coating as well the BCP buffer interlayer. The standard blade coater consists of a blade(also call knife or applicator) with a micrometer screw which allows tuning of heights between blade and substrate surface[39], and a mechanism to move the blade through the substrate surface. Standard blade coater limited the solvent evaporation to substrate temperature which produced very poor perovskite films at low temperatures; therefore, the blade coater was modified adding a nitrogen blower system developed by CSEM Brasil. The schematic designs of both standard and modified blade coater are shown in **Figure 1.a**. Hence, the perovskite absorber was printed using the blade coater assisted by a nitrogen blower to rapidly evaporate the DMF solvent and therefore obtain more compact films[10] as shown in **Figure 1.b**. The morphology of perovskite film was studied by optical, scanning electron, atomic force, and photoluminescence microscopies. Similarly, the challenging deposition of BCP was achieved by blade coating deposition instead of the customary thermal evaporation or spin coating techniques. BCP was coated for the first time in air using roll-to-roll compatible techniques.

2.1. Perovskite film formation:

In order to highlight the effect of blade coated BCP on the performance of resulting cells, the PEDOT:PSS and PCBM layer were deposited by blade coating, while the BCP interlayer was deposited via spin coating (reference device) and blade coating. The Ag electrode was thermally evaporated. The perovskite layer deposition was assisted

by a nitrogen drying process based on Di Giacomo et al [15] approach. Normally, the perovskite solution is blade coated on the glass substrate and then the solvent is removed by thermal annealing; however, this leads to a very rough and inhomogeneous films full of pinholes as shown in **Figure 1.b-c**. Therefore, a nitrogen drying methodology was implemented to obtain more compact and smooth films. A schematic design of this method is shown in **Figure 1.a.** The optical microscopies (at 100x) presented together with a photograph of final perovskite film in Figure 1 evidenced the effect of nitrogen drying in perovskite morphology. The films dried with nitrogen were smooth, semi-transparent, and highly compact with an average roughness (Ra) of 16.57±2.22 nm (Ra value was measured after deposition of PCBM and BCP using a profilometer). This effect could be attributed to the short time lapse between the deposition of perovskite and nitrogen drying which prevented the interaction between the perovskite wet film and water/oxygen molecules in the air[20]. In fact, the roughness of perovskite films dried with nitrogen was much lower than that of films deposited without any nitrogen drying (Ra values up to 152 µm). **Figure 1.d** shows a highly reflected perovskite film fabricated using the above-mentioned nitrogen drying methodology.

The quality of perovskite films was confirmed by X-ray diffraction (XRD), Raman and scanning electron microscopy (SEM) as shown by the results in **Figure 2**. The XRD measurements were carried out to further examine the perovskite crystal growth when using blade coating technique assisted by nitrogen drying. The **Figure 2.a** shows the XRD patterns of perovskite films deposited on ITO/PEDOT:PSS substrates. The perovskite films presented peaks at diffraction angles (2θ) of 14.12° and 28.25° corresponding to the characteristics (110) and (220) planes (respectively) of methylammonium lead trihalide perovskite ($CH_3NH_3PbI_3$) as reported elsewhere[40].

Furthermore, the very low intensity or even the no evidence of peaks at 21.8° and 17.5° indicate low water absorption during deposition since these peaks are characteristic for $CH_3NH_3PbI_3$:H_2O complexes[41]. Therefore, the diffraction results confirm the formation of highly oriented and crystalline films of tetragonal $CH_3NH_3PbI_3$ structure. Nevertheless, there is also evidence for remnants of $CH_3NH_3PbI_3$ precursors including PbI_2 (12.7°), and $CH_3NH_3PbI_{3-x}Cl_x$ (15.7°) [40]. It was evidenced that PbI_2 peaks were more intense when RH was higher than 40%; therefore, perovskite films were deposited only when RH was below that value with the champions cells being fabricated at relative humidity equal or below 35%. High humidity values (RH>40%) led to perovskite films with a surface full of PbI_2. PSC with an excess of PbI_2 shown faster degradation compare to those without for the well-known Ag/I interaction. Also, excess of PbI_2 could be controlled by tuning the deposition parameters during coating or even in thermal annealing of films[42]. SEM and Raman analysis were carried on to better understand the perovskite growth. The SEM image, in **Figure 2.b**, shows a well-covered perovskite film on ITO/PEDOT:PSS which are compact without pin-holes, being optimal for use in photovoltaic devices. The inset of **Figure 2.b** shows a zoom in of the film. The average crystal size was around 300 nm, consistent with that reported in the literature[43]–[46] for perovskite grown on PEDOT:PSS. The Raman spectrum (see **Figure 2.c**) shown the perovskite surface composition of films deposited over ITO/PEDOT:PSS when excited at 532 nm. The 119 cm^{-1} peak is attributed to $CH_3NH_3PbI_3$ thin film [47], [48] meanwhile the 76 cm^{-1} and 94 cm^{-1} to PbI_2 [48]–[50]. The presence of PbI_2 may be a result of unconverted PbI_2 precursor (derivate from $Pb(C_2H_3O_2)_2.3H_2O$ and CH_3NH_3I reaction[51]) from air-processed deposition or perovskite degradation[41]. Finally, the optical profile of blade-coated perovskite films allows the estimation of perovskite bandgap through the Tauc plot (**Figure 2.d**). It was assumed that perovskite

semiconductor has a direct band gap with an estimated energy gap of 1.6 eV which is comparable to those reported for tetragonal $CH_3NH_3PbI_3$ structures[52].

2.2. Perovskite Solar Cells performance:

BCP is commonly used as buffer layer in a p-i-n PSC acting as HBL[27] and reducing the recombination at the top electrode. BCP is a robust material which is very stable in air[53]; however, the thickness of BCP plays a critical role in PSC performance since thick BCP layers result in a very low FF whereas too thin layers are not effective in blocking recombination; therefore, thickness must be set between 5 and 7 nm[28]. BCP has been deposited either by spin coating inside of an inert atmosphere (i.e N_2 or Ar glovebox [33], [34]) or by thermal evaporation[37], [38] never by blade coating up till now. In most of these reports, the BCP film is deposited on extremely flat perovskite film fabricated by spin coating using the well-known Lewis adduct approach (use of anlti-solvent); however, when perovskite is deposited by blade coating, resulting film presents rougher surfaces than spin coated films with rough mean square (RMS) of at least 10 nm. Therefore, blade coated BCP films not only work as hole blocking barrier but also as planarization film reducing the RMS of $CH_3NH_3PbI_3$/PCBM films in a factor of 5 compare to spin coated films. The planarization is important due to the charge distribution at interfaces. In this aspect, flatter films would reduce charge accumulation and, consequently, recombination. Here the thickness of BCP film was controlled by varying the deposition speeds (5 -10 mm/s) of the blade with respect to the surface of the sample. PSCs without BCP and with a BCP layer deposited by a spin coating were fabricated as references. A cross-section SEM image of the resulting PSC is shown in **Figure 3.a** while the photovoltaic performance of cells are reported in **Table 1** and **Figure 3.b**.

Devices with spin coated BCP delivered a maximum PCE of 13.6%. The cells with blade coated BCP delivered an even higher PCE of 14.9 % and 14.4% at deposition speeds of 5 mm/s and 10 mm/s, respectively. However, it is important to clarify that cells with spin coated BCP in air reached the maximum PCE when they were fresh (PCE was measured immediately after Ag evaporation), and blade coated cells did it after one day inside a cabinet filled with pure nitrogen which maintained the RH below 10% (Figure 3.d). This improvement could be attributed to the evaporation of remaining solvent within the BCP film which could act as charge traps at the interfaces PCBM/BCP or BCP/Ag. Once solvent is fully evaporated, the charge traps are reduced[54] leading to an increase of fill factor from 68% in fresh devices to 70% after 1 day. This effect is not evidenced in spin coated devices since solvent evaporation dynamic of each the deposition technique is different. **Figure 4** shows a schematic design of BCP deposition using either solution processes including blade and spin coating or thermal evaporation. Thermal evaporated films cover the $CH_3NH_3PbI_3$/PBCM substrate, following the rough morphology and forming homogeneous compact films. However, in the solution processes, the morphology of film will depend on how the excess of solvent is removed. For spin coated films, the most volume of total solution is ejected when centrifugation starts, and the small amounts of remaining solvent are rapidly evaporated by the air flow produced by the spin process itself[55], [56]. Therefore, deposition on rough substrate led the solution to fill the valleys while peaks remained uncoated. Contrary, in the blade coating process the deposition has two steps: 1) wet film deposition and 2) solvent evaporation. Low deposition speeds (comparing to very fast spin deposition speeds) allows that solution cover the rough surfaces uniformly, since the solvent evaporation occurs only after the deposition by natural drying (induced by plate temperature or air flow) being much slower compare to the spin coating.[57], [58] Additionally, fresh devices, either with spin coated

or blade coated BCP, presented negligible hysteresis with even a slightly higher PCE in forward scan than in reverse. Negligible hysteresis means that PSCs are stable because the cells are free of superficial-traps[59]. Stability was also tested under continuous light soaking. Spin coated BCP based cells reached a stabilized PCE 10% (in relative terms) higher than the initial PCE after 18 min of 1-sun irradiation due to an enhancement of FF mainly due to the PCBM/BCP interlayer passivation or reduction of interface charge accumulation[28], [60], [61]. For blade coated BCP based cells, the PCE was constant through time. The cells presented good reproducibility and stability (**Figure 3.c-d**) with average PCE of 11.67±1.51% and 13.10±0.97% (over 12 cells) for spin coated and blade coated BCP respectively. The PCE of blade coated PSC were, in relative terms, 79% higher than those without BCP. Also, PSCs with blade coated BCP retained 74% (in relative terms) of initial PCE after one month without any encapsulation and stored in dark inside of a nitrogen cabinet with RH<15%. Additionally, in an interlaboratory collaboration, encapsulated samples were sent from Brazil to Italy presenting negligible degradation. The interlaboratory collaboration was aimed at evaluating the difference devices architectures with transient photovoltage (TPV), transient photocurrent (TPV), electroluminescence (EL) and external quantum efficiency (EQE) tests, and results are presented in **Figure 5**. EQE measurements evidenced that BCP improved the charge extraction since spectrum intensities were higher for the full wavelength range reaching maximum intensities when BCP was deposited by blade coating. EQE enhanced possibly was the result of a reduction of radiative recombination or a better charge generation; therefore, electron-luminescence (EL) test, transient photovoltage (TPV) and transient photocurrent (TPC) test were carried out on full PSCs to understand this improvement and results are plotted in **Figure 5b-d**. EL results shown a quenching effect of BCP which was higher for film deposited by blade coating than spin coating. Quenching indicated a reduction of radiative recombination

induced for the charge carrier extraction properties of the BCP/Ag cathode[62]. TPV tests allowed the calculation of charge carrier lifetimes which presented a low decay (electron–hole recombination) for BCP based devices[63]. Also, TCP shown that PSC with blade coated BCP film had the best extracted charge density. The difference between spin and bladed coated BCP buffer was studied also by dark current measurements (**Figure 6.a**). All cells presented high behavior (Jon/Joff) except for cells without BCP, meaning that cells had efficient selective contacts in charge extraction as well as limiting recombination close to the electrodes. The Jon/Joff values were 358, 326 and 1 for spin coated, blade coated (at 5mm/s), and without the BCP layer, respectively. The addition of BCP interlayer reduced charge recombination and therefore improved the rectification values by at least 2 order of magnitude. Nevertheless, the cells with a blade coated BCP had a quite higher current density at 0.5 V than cells based on spin coated BCP. This effect could be generated by deep traps which produced charge recombination[64]–[66].

The electrical characterization of PSCs has shown that blade coating deposition was a better option than spin coating for BCP deposition in air. Consequently, PSCs were characterized using photoluminescent mapping and atomic force microscopic to correlate the deposition technique and PSC performance. The reason behind the PCE improvement of PSC incorporating a blade coated BCP films respect to those with spin coated one can be mainly ascribed to the surface morphology of BCP hole blocking layer itself.

The photoluminescence spectra of the ITO/PEDOT:PSS/$CH_3NH_3PbI_3$/PCBM/BCP films with the HBL deposited by spin and blade coating are show in **Figure 6.b** and the respective scanning confocal PL maps are presented in **Figure 6.c** and in **Figure 6.d**. The PL spectra of each sample were measure in two different points A and B. Since PEDOT:PSS, perovskite and PCBM films were deposited using the same parameters, it is assumed that the reduction in the intensity of

PL peak corresponds only to the quenching induced by the BCP layer. Then, comparing the PL quenching when introducing the BCP processed by blade or spin coating, it is observed that the BCP processed by blade coating had high homogeneity since PL peaks at both A and B points presented similar intensities. Thus, blade coated BCP highly improved the PL quenching by decreasing the radiative charge recombination process at the perovskite/electrode interface. This is a positive effect since it has already been proven that the interface between the absorber and transport layers directly affects solar cell performance[67]. Contrarily, the spin coated BCP (**Figure 6.c**) had a poor covering showing greatly different between point A and B (being A where BCP is placed (with higher quenching than B). The scanning confocal PL maps show that, besides the optical submicrometer heterogeneities of perovskite films[68], the PL quenching is more evident in the BCP by blade coating than by spin coating. Therefore, atomic force microscopy (AFM) measurements were carried out to compare the morphology of BCP films deposited by spin and blade coating. The height contrast observed in **Figure 7** is related to the superficial topographic of films. The AFM images in **Figure 7.a** and **Figure 7.b** clearly show an effective planarization of perovskite film when BCP films was processed by blade coating (better covering than spin coated films). The RMS of BCP films by blade coating on $CH_3NH_3PbI_3$/PCBM was 2 nm being 5 time lower than spin coated films. The smooth surface of the interlayer is beneficial to reduce the resistance and accelerating the charge transport[69], which directly affect FF and device performance. PL and AFM results proved the solvent drying hypothesis presented in **Figure 4**. Kelvin probe force microscopy (KPFM) was carried out simultaneously to height contrast. The Kelvin probe is a tool to measure the work function (W) of films. The contrast of images **Figure 7.c** and **Figure 7.d** is related to the voltage applied in the probe to suppress the difference between the W_{probe} and W_{film}[70]. Consequently, a lower voltage contrast of

ITO/PEDOT:PSS/$CH_3NH_3PbI_3$/PCBM/BCP films is observed in blade coating processed layers compared to those in spin coating. (**Figure 7**.c and **Figure 7**.d. respectively). These results confirm the optimal morphology of totally blade coated BCP films. Finally, this work presented the advantage of printed BCP buffer layer against traditional spin coated methodology. PSCs delivered PCE up to 15% (in 0.5 cm^2); nevertheless, some relevant aspects should be improved before PSC R2R manufacturing. The increase of active area will drop the PCE since sheet resistance of transparent conductive oxides (TCO) will increase; therefore, more conductive TCO such us ITO/metal/ITO (IMI) or indium zinc oxide (IZO) must be studied since they could reduce the series resistance[71]. Also, the implementation of multication perovskites will also lead to high performing devices. For example, the addition of Cs+ could enhanced the PCE in a 15% (in relative terms) and the long term stability[72]. Finally, the use of more efficient charge transport layer including Poly[bis(4-phenyl)(2,4,6-trimethylphenyl)amine (PTAA) or nickel oxide (NiO) could lead to an increase of FF and Voc which will raise the performance[73], [74].

3. CONCLUSION

In conclusion, we have fabricated a fully printed perovskite solar cells in air via the blade coating technique incorporating a nanometer-thick BCP buffer layer. The nanometer-thick BCP interlayer was successfully deposited for the first time via blade coating in air. The PCE of PSC with blade coated BCP were 10% higher than their counterpart with spin coated BCP and 63% higher than those without any BCP layer delivering maximum PCEs of 14.9%, 13.6% and 9.1% respectively. Also, through optical and structural analysis, we have probed that the solar cell with BCP processed by blade coating showed better charge transport at absorber/interlayer interface due to a flatter film than by spin coating. These results firmly indicate that BCP deposited by methods closer

to large area production can produce even higher performance than the well-known spin coating technique. Also, thermally evaporated BCP have been recently deposited on blade coated multiple-cation perovskites (PCE~22%); therefore, BCP deposition by blade coating should be optimized on high efficiency multiple-cation based PSCs. Finally, the deposition of BCP also shows that very thin films can be deposited by blade coating and therefore can be applied, for example, to the deposition of other layers such as PTAA (~8 nm [2]) to replace the PEDOT:PSS, or to deposit nanometer-thick electron transport or hole blocking layer such as C60 or MgO, respectively, enhancing the PCE of fully printed PSCs. This approach demonstrated the deposition of BCP by blade-coating instead of highly energy cost vacuum process (thermal evaporation) proving the compatibility of this nanometer-thick interlayer with R2R processes and paving the way for further investigations for cells incorporating BCP by slot-die

ACKNOWLEDGEMENTS

We acknowledge Petróleo Brasileiro S.A. (PETROBRAS) under the project "Research and Development of Perovskite formulations for production of printed photovoltaic cells and modules" for funding. S.C.H and T.M.B acknowledge to have received funding from Departamento del Huila's Scholarship Program No. 677 from Huila, Colombia, the European Union's Horizon 2020 research and innovation program under grant agreement no. 763989 APOLO, Lazio Region "Gruppi di Ricerca" under project no. 85-2017-15373 (SIROH) according to L.R. Lazio 13/08, and the Italian Ministry of University and Research (MIUR) through the PRIN2017 BOOSTER (project n.2017YXX8AZ) grant. This publication reflects only the authors' views and the funding agencies are not liable for any use that may be made of the information contained therein. We thank to Gabriela Amorim for solar cell encapsulation. We thank engineering department at CSEM Brasil for developing the nitrogen blower system. We thank to Centro de Microscopia, Laboratório de Caracterização e de Processamento de Nanomateriais from Federal University of Minas Gerais, for providing the experimental facilities and Prof. Wagner da Nova Mussel for XRD results.

REFERENCES

[1] National Renewable Enery Laboratory, "Best Research-Cell Efficiencies," *https://www.nrel.gov/pv/cell-efficiency.html*, 2019. https://www.nrel.gov/pv/cell-efficiency.html.

[2] M. Saliba *et al.*, "How to Make over 20% Efficient Perovskite Solar Cells in Regular (n-i-p) and Inverted (p-i-n) Architectures," *Chem. Mater.*, vol. 30, no. 13, pp. 4193–4201, 2018, doi: 10.1021/acs.chemmater.8b00136.

[3] I. Burgués-Ceballos, M. Stella, P. Lacharmoise, and E. Martínez-Ferrero, "Towards industrialization of polymer solar cells: material processing for upscaling," *J. Mater. Chem. A*, vol. 2, no. 42, pp. 17711–17722, 2014, doi: 10.1039/C4TA03780D.

[4] F. Huang, M. Li, P. Siffalovic, G. Cao, and J. Tian, "From scalable solution fabrication of perovskite films towards commercialization of solar cells," *Energy Environ. Sci.*, vol. 12, no. 2, pp. 518–549, 2019, doi: 10.1039/C8EE03025A.

[5] S. Razza, S. Castro-Hermosa, A. Di Carlo, and T. M. Brown, "Research Update: Large-area deposition, coating, printing, and processing techniques for the upscaling of perovskite solar cell technology," *APL Mater.*, vol. 4, no. 9, p. 091508, Sep. 2016, doi: 10.1063/1.4962478.

[6] M. Yang *et al.*, "Perovskite ink with wide processing window for scalable high-efficiency solar cells," *Nat. Energy*, vol. 2, no. March, p. 17038, 2017, doi: 10.1038/nenergy.2017.38.

[7] Y. Galagan *et al.*, "Roll-to-Roll Slot Die Coated Perovskite for Efficient Flexible Solar Cells," *Adv. Energy Mater.*, vol. 1801935, p. 1801935, Oct. 2018, doi:

10.1002/aenm.201801935.

[8] B. Dou *et al.*, “Roll-to-Roll Printing of Perovskite Solar Cells,” *ACS Energy Lett.*, vol. 3, no. 10, pp. 2558–2565, Oct. 2018, doi: 10.1021/acsenergylett.8b01556.

[9] J. B. Whitaker *et al.*, “Scalable slot-die coating of high performance perovskite solar cells,” *Sustain. Energy Fuels*, 2018, doi: 10.1039/C8SE00368H.

[10] N. Ahn, D.-Y. Y. Son, I.-H. H. Jang, S. M. Kang, M. Choi, and N.-G. G. Park, “Highly Reproducible Perovskite Solar Cells with Average Efficiency of 18.3% and Best Efficiency of 19.7% Fabricated via Lewis Base Adduct of Lead(II) Iodide,” *J. Am. Chem. Soc.*, vol. 137, no. 27, pp. 8696–8699, Jul. 2015, doi: 10.1021/jacs.5b04930.

[11] H. Uratani and K. Yamashita, “Charge Carrier Trapping at Surface Defects of Perovskite Solar Cell Absorbers: A First-Principles Study,” *J. Phys. Chem. Lett.*, vol. 8, no. 4, pp. 742–746, 2017, doi: 10.1021/acs.jpclett.7b00055.

[12] Y.-H. Seo, E.-C. Kim, S.-P. Cho, S.-S. Kim, and S.-I. Na, “High-performance planar perovskite solar cells: Influence of solvent upon performance,” *Appl. Mater. Today*, vol. 9, pp. 598–604, 2017, doi: 10.1016/j.apmt.2017.11.003.

[13] J. Li *et al.*, “Phase Transition Control for High-Performance Blade-Coated Perovskite Solar Cells,” *Joule*, vol. 2, no. 7, pp. 1313–1330, Jul. 2018, doi: 10.1016/j.joule.2018.04.011.

[14] Z. Yang, C.-C. Chueh, F. Zuo, J. H. Kim, P.-W. Liang, and A. K.-Y. Jen, “High-Performance Fully Printable Perovskite Solar Cells via Blade-Coating Technique under the Ambient Condition,” *Adv. Energy Mater.*, vol. 5, no. 13, p. 1500328,

Jul. 2015, doi: 10.1002/aenm.201500328.

[15] F. Di Giacomo *et al.*, “Up-scalable sheet-to-sheet production of high efficiency perovskite module and solar cells on 6-in. substrate using slot die coating,” *Sol. Energy Mater. Sol. Cells*, vol. 181, no. August, pp. 53–59, Jul. 2018, doi: 10.1016/j.solmat.2017.11.010.

[16] W. Zhang *et al.*, “Ultrasmooth organic-inorganic perovskite thin-film formation and crystallization for efficient planar heterojunction solar cells,” *Nat. Commun.*, vol. 6, 2015, doi: 10.1038/ncomms7142.

[17] C. Li *et al.*, “Efficient lead acetate sourced planar heterojunction perovskite solar cells with enhanced substrate coverage via one-step spin-coating,” *Org. Electron. physics, Mater. Appl.*, vol. 33, pp. 194–200, 2016, doi: 10.1016/j.orgel.2016.03.017.

[18] F. K. Aldibaja, L. Badia, E. Mas-Marzá, R. S. Sánchez, E. M. Barea, and I. Mora-Sero, “Effect of different lead precursors on perovskite solar cell performance and stability,” *J. Mater. Chem. A*, vol. 3, no. 17, pp. 9194–9200, 2015, doi: 10.1039/C4TA06198E.

[19] W. Qiu *et al.*, “Pinhole-free perovskite films for efficient solar modules,” *Energy Environ. Sci.*, vol. 9, no. 2, pp. 484–489, 2016, doi: 10.1039/C5EE03703D.

[20] W. Kong *et al.*, “Fabricating High-Efficient Blade-Coated Perovskite Solar Cells under Ambient Condition Using Lead Acetate Trihydrate,” *Sol. RRL*, vol. 2, no. 3, p. 1700214, Mar. 2018, doi: 10.1002/solr.201700214.

[21] J.-E. Kim *et al.*, “Slot die coated planar perovskite solar cells via blowing and heating assisted one step deposition,” *Sol. Energy Mater. Sol. Cells*, vol. 179, no.

January, pp. 80–86, Jun. 2018, doi: 10.1016/j.solmat.2018.02.003.

[22] G. Cotella *et al.*, "One-step deposition by slot-die coating of mixed lead halide perovskite for photovoltaic applications," *Sol. Energy Mater. Sol. Cells*, vol. 159, pp. 362–369, 2017, doi: 10.1016/j.solmat.2016.09.013.

[23] M. Kohlstädt, M. A. Yakoob, and U. Würfel, "A Matter of Drying: Blade-Coating of Lead Acetate Sourced Planar Inverted Perovskite Solar Cells on Active Areas >1 cm 2," *Phys. status solidi*, vol. 215, no. 21, p. 1800419, Nov. 2018, doi: 10.1002/pssa.201800419.

[24] F. Matteocci *et al.*, "Solid-state solar modules based on mesoscopic organometal halide perovskite: a route towards the up-scaling process.," *Phys. Chem. Chem. Phys.*, vol. 16, no. 9, pp. 3918–3923, 2014, doi: 10.1039/c3cp55313b.

[25] Q. Zhao, G. R. Li, J. Song, Y. Zhao, Y. Qiang, and X. P. Gao, "Improving the photovoltaic performance of perovskite solar cells with acetate," *Sci. Rep.*, vol. 6, no. 1, p. 38670, Dec. 2016, doi: 10.1038/srep38670.

[26] J. Ye *et al.*, "Enhanced morphology and stability of high-performance perovskite solar cells with ultra-smooth surface and high fill factor via crystal growth engineering," *Sustain. Energy Fuels*, vol. 1, no. 4, pp. 907–914, 2017, doi: 10.1039/C7SE00036G.

[27] T. Liu, K. Chen, Q. Hu, R. Zhu, and Q. Gong, "Inverted Perovskite Solar Cells: Progresses and Perspectives," *Adv. Energy Mater.*, vol. 6, no. 17, p. 1600457, Sep. 2016, doi: 10.1002/aenm.201600457.

[28] C. Chen *et al.*, "Effect of BCP buffer layer on eliminating charge accumulation for high performance of inverted perovskite solar cells," *RSC Adv.*, vol. 7, no. 57,

pp. 35819–35826, 2017, doi: 10.1039/c7ra06365b.

[29] J. Dagar, S. Castro-Hermosa, G. Lucarelli, A. Zampetti, F. Cacialli, and T. M. Brown, “Low-Temperature Solution-Processed Thin SnO2/Al2O3 Double Electron Transport Layers Toward 20% Efficient Perovskite Solar Cells,” *IEEE J. Photovoltaics*, vol. 9, no. 5, pp. 1309–1315, Sep. 2019, doi: 10.1109/JPHOTOV.2019.2928466.

[30] J. Dagar, S. Castro-Hermosa, G. Lucarelli, F. Cacialli, and T. M. Brown, “Highly efficient perovskite solar cells for light harvesting under indoor illumination via solution processed SnO2/MgO composite electron transport layers,” *Nano Energy*, vol. 49, no. June, pp. 290–299, Jul. 2018, doi: 10.1016/j.nanoen.2018.04.027.

[31] W. Q. Wu, P. N. Rudd, Q. Wang, Z. Yang, and J. Huang, “Blading Phase-Pure Formamidinium-Alloyed Perovskites for High-Efficiency Solar Cells with Low Photovoltage Deficit and Improved Stability,” *Adv. Mater.*, vol. 2000995, pp. 1–8, 2020, doi: 10.1002/adma.202000995.

[32] W. Q. Wu *et al.*, “Reducing Surface Halide Deficiency for Efficient and Stable Iodide-Based Perovskite Solar Cells,” *J. Am. Chem. Soc.*, vol. 142, no. 8, pp. 3989–3996, 2020, doi: 10.1021/jacs.9b13418.

[33] C. Stenta, M. P. Montero-Rama, A. Viterisi, W. Cambarau, E. Palomares, and L. F. Marsal, “Solution Processed Bathocuproine for Organic Solar Cells,” *IEEE Trans. Nanotechnol.*, vol. 17, no. 1, pp. 128–132, Jan. 2018, doi: 10.1109/TNANO.2017.2779544.

[34] K. Cao *et al.*, “Phosphor coated NiO-based planar inverted organometallic halide perovskite solar cells with enhanced efficiency and stability,” *Appl. Phys. Lett.*,

vol. 109, no. 17, p. 171103, 2016, doi: 10.1063/1.4965838.

[35] Y. Wang *et al.*, “Solution-processed bathocuproine cathode buffer layer towards efficient planar heterojunction perovskite solar cells,” *Semicond. Sci. Technol.*, vol. 34, no. 7, p. 075023, Jul. 2019, doi: 10.1088/1361-6641/ab2309.

[36] D. X. Yuan *et al.*, “A solution-processed bathocuproine cathode interfacial layer for high-performance bromine-iodine perovskite solar cells,” *Phys. Chem. Chem. Phys.*, vol. 17, no. 40, pp. 26653–26658, 2015, doi: 10.1039/c5cp03995a.

[37] M. He *et al.*, “Meniscus-assisted solution printing of large-grained perovskite films for high-efficiency solar cells,” *Nat. Commun.*, vol. 8, no. May, p. 16045, Jul. 2017, doi: 10.1038/ncomms16045.

[38] Y. Deng, X. Zheng, Y. Bai, Q. Wang, J. Zhao, and J. Huang, “Surfactant-controlled ink drying enables high-speed deposition of perovskite films for efficient photovoltaic modules,” *Nat. Energy*, 2018, doi: 10.1038/s41560-018-0153-9.

[39] S. Razza, S. Castro-Hermosa, A. Di Carlo, and T. M. Brown, “Research Update: Large-area deposition, coating, printing, and processing techniques for the upscaling of perovskite solar cell technology,” *APL Mater.*, vol. 4, no. 9, pp. 091508–15, Sep. 2016, doi: 10.1063/1.4962478.

[40] Y. Yan, W. J. Yin, T. Shi, W. Meng, and C. Feng, *Defect physics of CH3NH3PbX3 (X=I, Br, Cl) perovskites*. 2016.

[41] J. Schlipf *et al.*, “Shedding Light on the Moisture Stability of 3D/2D Hybrid Perovskite Heterojunction Thin Films,” *ACS Appl. Energy Mater.*, vol. 2, no. 2, pp. 1011–1018, Feb. 2019, doi: 10.1021/acsaem.9b00005.

[42] J. an Yang *et al.*, “Precise control of PbI2 excess into grain boundary for efficacious charge extraction in off-stoichiometric perovskite solar cells,” *Electrochim. Acta*, vol. 338, p. 135697, 2020, doi: 10.1016/j.electacta.2020.135697.

[43] X. Ren *et al.*, “Modulating crystal grain size and optoelectronic properties of perovskite films for solar cells by reaction temperature,” *Nanoscale*, vol. 8, no. 6, pp. 3816–3822, 2016, doi: 10.1039/C5NR08935B.

[44] Z. Liang *et al.*, “A large grain size perovskite thin film with a dense structure for planar heterojunction solar cells via spray deposition under ambient conditions,” *RSC Adv.*, vol. 5, no. 74, pp. 60562–60569, 2015, doi: 10.1039/C5RA09110A.

[45] J. Yun *et al.*, “Highly efficient perovskite solar cells incorporating NiO nanotubes: increased grain size and enhanced charge extraction,” *J. Mater. Chem. A*, vol. 5, no. 41, pp. 21750–21756, 2017, doi: 10.1039/C7TA05560A.

[46] G. Lu, W. Zhu, F. He, D. Chen, C. Zhang, and Y. Hao, “Enhanced sensitivity of grain sizes to precursor stoichiometry enables high-quality CH3NH3PbI3 films for efficient perovskite solar cells,” *Mater. Lett.*, vol. 250, pp. 88–91, Sep. 2019, doi: 10.1016/j.matlet.2019.04.127.

[47] C. Quarti *et al.*, “The raman spectrum of the CH3NH3PbI3 hybrid perovskite: Interplay of theory and experiment,” *J. Phys. Chem. Lett.*, vol. 5, no. 2, pp. 279–284, 2014, doi: 10.1021/jz402589q.

[48] P. Pistor, A. Ruiz, A. Cabot, and V. Izquierdo-Roca, “Advanced Raman Spectroscopy of Methylammonium Lead Iodide: Development of a Non-destructive Characterisation Methodology,” *Sci. Rep.*, vol. 6, no. April, pp. 1–8, 2016, doi: 10.1038/srep35973.

[49] Y. Xie, F. Shao, Y. Wang, T. Xu, D. Wang, and F. Huang, “Enhanced Performance of Perovskite CH3NH3PbI3 Solar Cell by Using CH3NH3I as Additive in Sequential Deposition,” *ACS Appl. Mater. Interfaces*, vol. 7, no. 23, pp. 12937–12942, 2015, doi: 10.1021/acsami.5b02705.

[50] W. Kong, A. Rahimi-Iman, G. Bi, X. Dai, and H. Wu, “Oxygen Intercalation Induced by Photocatalysis on the Surface of Hybrid Lead Halide Perovskites,” *J. Phys. Chem. C*, vol. 120, no. 14, pp. 7606–7611, 2016, doi: 10.1021/acs.jpcc.6b00496.

[51] A. S. Yerramilli, Y. Chen, D. Sanni, J. Asare, N. D. Theodore, and T. L. Alford, “Impact of excess lead on the stability and photo-induced degradation of lead halide perovskite solar cells,” *Org. Electron. physics, Mater. Appl.*, vol. 59, no. April, pp. 107–112, 2018, doi: 10.1016/j.orgel.2018.04.052.

[52] T. Baikie *et al.*, “Synthesis and crystal chemistry of the hybrid perovskite (CH 3NH3)PbI3 for solid-state sensitised solar cell applications,” *J. Mater. Chem. A*, vol. 1, no. 18, pp. 5628–5641, 2013, doi: 10.1039/c3ta10518k.

[53] X. Sun *et al.*, “Room-temperature air-stable spin transport in bathocuproine-based spin valves,” *Nat. Commun.*, vol. 4, no. May, pp. 1–7, 2013, doi: 10.1038/ncomms3794.

[54] A. K. Chauhan *et al.*, “Interfacial charge trapping in the polymer solar cells and its elimination by solvent annealing,” *AIP Adv.*, vol. 6, no. 9, 2016, doi: 10.1063/1.4963014.

[55] F. C. Krebs, “Fabrication and processing of polymer solar cells: A review of printing and coating techniques,” *Sol. Energy Mater. Sol. Cells*, vol. 93, no. 4, pp. 394–412, 2009, doi: 10.1016/j.solmat.2008.10.004.

[56] B. T. Chen, “Investigation of the solvent-evaporation effect on spin coating of thin films,” *Polym. Eng. Sci.*, vol. 23, no. 7, pp. 399–403, May 1983, doi: 10.1002/pen.760230706.

[57] C.-H. Jun, S. Ohisa, Y.-J. Pu, T. Chiba, and J. Kido, “Comparison of Spin and Blade Coating Methods in Solution-process for Organic Light-emitting Devices,” *J. Photopolym. Sci. Technol.*, vol. 28, no. 3, pp. 343–347, 2015, doi: 10.2494/photopolymer.28.343.

[58] N. Park and K. Zhu, “Scalable fabrication and coating methods for perovskite solar cells and solar modules,” *Nat. Rev. Mater.*, Feb. 2020, doi: 10.1038/s41578-019-0176-2.

[59] B. Chen, M. Yang, S. Priya, and K. Zhu, “Origin of J – V Hysteresis in Perovskite Solar Cells,” *J. Phys. Chem. Lett.*, vol. 7, no. 5, pp. 905–917, Mar. 2016, doi: 10.1021/acs.jpclett.6b00215.

[60] X. Li *et al.*, “Passivation against oxygen and light induced degradation by the PCBM electron transport layer in planar perovskite solar cells,” *Sustain. Energy Fuels*, vol. 2, no. 8, pp. 1686–1692, 2018, doi: 10.1039/c8se00095f.

[61] Y. Shao, Z. Xiao, C. Bi, Y. Yuan, and J. Huang, “Origin and elimination of photocurrent hysteresis by fullerene passivation in CH3NH3PbI3planar heterojunction solar cells,” *Nat. Commun.*, vol. 5, pp. 1–7, 2014, doi: 10.1038/ncomms6784.

[62] J. Dagar *et al.*, “Efficient fully laser-patterned flexible perovskite modules and solar cells based on low-temperature solution-processed SnO2/mesoporous-TiO2 electron transport layers,” *Nano Res.*, vol. 11, no. 5, pp. 2669–2681, May 2018, doi: 10.1007/s12274-017-1896-5.

[63] D. Tsikritzis *et al.*, " A two-fold engineering approach based on Bi 2 Te 3 flakes towards efficient and stable inverted perovskite solar cells ," *Mater. Adv.*, vol. 1, no. 3, pp. 450–462, 2020, doi: 10.1039/d0ma00162g.

[64] U. K. Thakur, A. M. Askar, R. Kisslinger, B. D. Wiltshire, P. Kar, and K. Shankar, "Halide perovskite solar cells using monocrystalline TiO 2 nanorod arrays as electron transport layers: impact of nanorod morphology," *Nanotechnology*, vol. 28, no. 27, p. 274001, Jul. 2017, doi: 10.1088/1361-6528/aa75ab.

[65] X. Ji *et al.*, "2.6 μm MBE grown InGaAs detectors with dark current of SRH and TAT," *AIP Adv.*, vol. 4, no. 8, pp. 0–7, 2014, doi: 10.1063/1.4894142.

[66] G. A. H. Wetzelaer, M. Kuik, M. Lenes, and P. W. M. Blom, "Origin of the dark-current ideality factor in polymer:fullerene bulk heterojunction solar cells," *Appl. Phys. Lett.*, vol. 99, no. 15, pp. 2011–2014, 2011, doi: 10.1063/1.3651752.

[67] J. Carrillo *et al.*, "Ionic Reactivity at Contacts and Aging of Methylammonium Lead Triiodide Perovskite Solar Cells," *Adv. Energy Mater.*, vol. 6, no. 9, pp. 1–7, 2016, doi: 10.1002/aenm.201502246.

[68] D. Moerman, G. E. Eperon, J. T. Precht, and D. S. Ginger, "Correlating Photoluminescence Heterogeneity with Local Electronic Properties in Methylammonium Lead Tribromide Perovskite Thin Films," *Chem. Mater.*, vol. 29, no. 13, pp. 5484–5492, 2017, doi: 10.1021/acs.chemmater.7b00235.

[69] R. D. Chavan, P. Yadav, A. Nimbalkar, S. P. Bhoite, P. N. Bhosale, and C. Kook Hong, "Ruthenium doped mesoporous titanium dioxide for highly efficient, hysteresis-free and stable perovskite solar cells," *Sol. Energy*, vol. 186, no. February, pp. 156–165, 2019, doi: 10.1016/j.solener.2019.04.098.

[70] J. Hidalgo, A. Castro-Méndez, and J. Correa-Baena, “Imaging and Mapping Characterization Tools for Perovskite Solar Cells,” *Adv. Energy Mater.*, vol. 1900444, p. 1900444, 2019, doi: 10.1002/aenm.201900444.

[71] B. Dou *et al.*, “High-Performance Flexible Perovskite Solar Cells on Ultrathin Glass: Implications of the TCO,” *J. Phys. Chem. Lett.*, vol. 8, no. 19, pp. 4960–4966, Oct. 2017, doi: 10.1021/acs.jpclett.7b02128.

[72] M. Saliba *et al.*, “Cesium-containing triple cation perovskite solar cells: improved stability, reproducibility and high efficiency,” *Energy Environ. Sci.*, vol. 9, no. 6, pp. 1989–1997, 2016, doi: 10.1039/C5EE03874J.

[73] N. G. Park, “Research Direction toward Scalable, Stable, and High Efficiency Perovskite Solar Cells,” *Adv. Energy Mater.*, vol. 1903106, pp. 1–14, 2019, doi: 10.1002/aenm.201903106.

[74] D. Di Girolamo *et al.*, “Stability and Dark Hysteresis Correlate in NiO-Based Perovskite Solar Cells,” *Adv. Energy Mater.*, vol. 9, no. 31, pp. 1–10, 2019, doi: 10.1002/aenm.201901642.

Table 1. Photovoltaic parameters of perovskite solar cells with PEDOT:PSS/ $CH_3NH_3PbI_3$/PCBM blade coated layers without BCP and with the BCP film deposited either by spin or blade coating.

BCP Deposition	Voc [V]	Jsc [mA/cm2]	FF [%]	PCE [%]
Without	0.91±0.09	19.08±2.26	41.56±3.03	7.28±1.38
Spin Coating	1.01±0.03	19.45±1.15	59.16±5.61	11.67±1.51
Blade Coating	1.01±0.01	19.89±1.24	65.14±4.04	13.10±0.97

Figure 1. (a) Schematic of perovskite deposition using standard (1) and nitrogen assisted (2) blade coating technique. (b) Photographs and (c) optical microscopies at 100x magnification of perovskite films deposited without (left) or with (right) nitrogen drying. (d) Perovskite film reflecting a CSEM Brasil organic photovoltaic module.

Figure 2. (a) X-ray diffraction pattern of perovskite growth at ambient conditions. (b) Morphological characterization of perovskite film obtained through a top view SEM image. (c) Raman spectra of perovskite films. (d) Absorption spectra of perovskite film. The red line corresponds to the absorption edge of Perovskite film. Considering the Tauc plot, the energy of band gap is 1.6 eV.

Figure 3. (a) Cross-section SEM image of a PSC fully printed in air with Glass/ITO/PEDOT:PSS/$CH_3NH_3PbI_3$/PCBM/BCP/Ag architecture. (b) Current-voltage curves of PSCs: red line corresponds to the PSC with spin coated BCP, blue line to the PSC optimized with blade coated BCP and the black line to samples without BCP. PEDOT:PSS, $CH_3NH_3PbI_3$ and PCBM were deposited by blade coating. (c) Statistics of 12 different cells of each kind of sample (d) J-V curves of best PSC with PEDOT:PSS, $CH_3NH_3PbI_3$ PCBM and BCP layers printed by blade coater after one day, four days and one month kept in dark at 23°C and 15% RH without encapsulation.

Figure 4. Schematic design of bathocuproine (BCP) deposition via blade coating, spin coating or thermal evaporation. Black arrow indicated the deposition direction.

Figure 5. (a) External quantum efficiency (EQE) and (b) Electroluminescence (EL) spectra of PSC without BCP (black line) and with BCP deposited by spin (red line) or blade coating (blue line). (c) Charge accumulation and (d) charge carrier lifetime extracted from transient photocurrent (TPC) and photovoltage (TPV) decays, respectively.

Figure 6. (a) J-V curves in dark of PSC without BCP (black line) and with BCP deposited by spin (red line) or blade coating (blue line). PL spectra (b), and PL mapping of Glass/ITO/PEDOT:PSS/CH3NH3PbI3/PCBM/BCP devices when BCP was deposited by spin (c) or blade (d) coating.

Figure 7. Atomic force microscopy (AFM) images of BCP films deposited on Glass/ITO/PEDOT:PSS/CH3NH3PbI3/PCBM by either spin (a, c) or blade coating (b, d). The first and second rows show the height and voltage contrast, respectively.

Figure 1

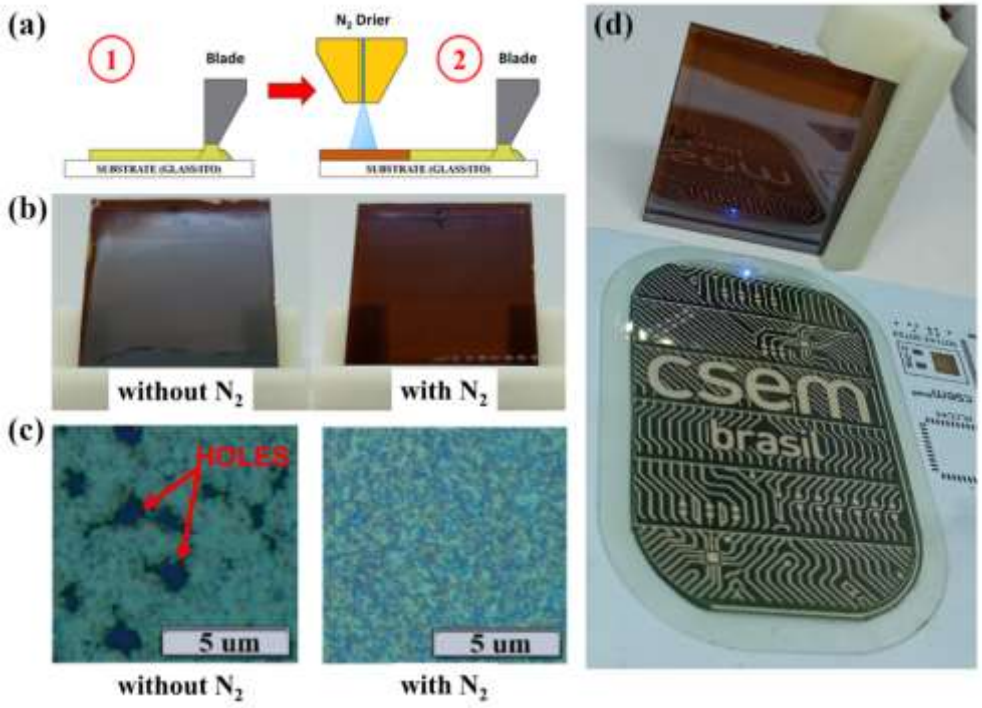

Figure 2

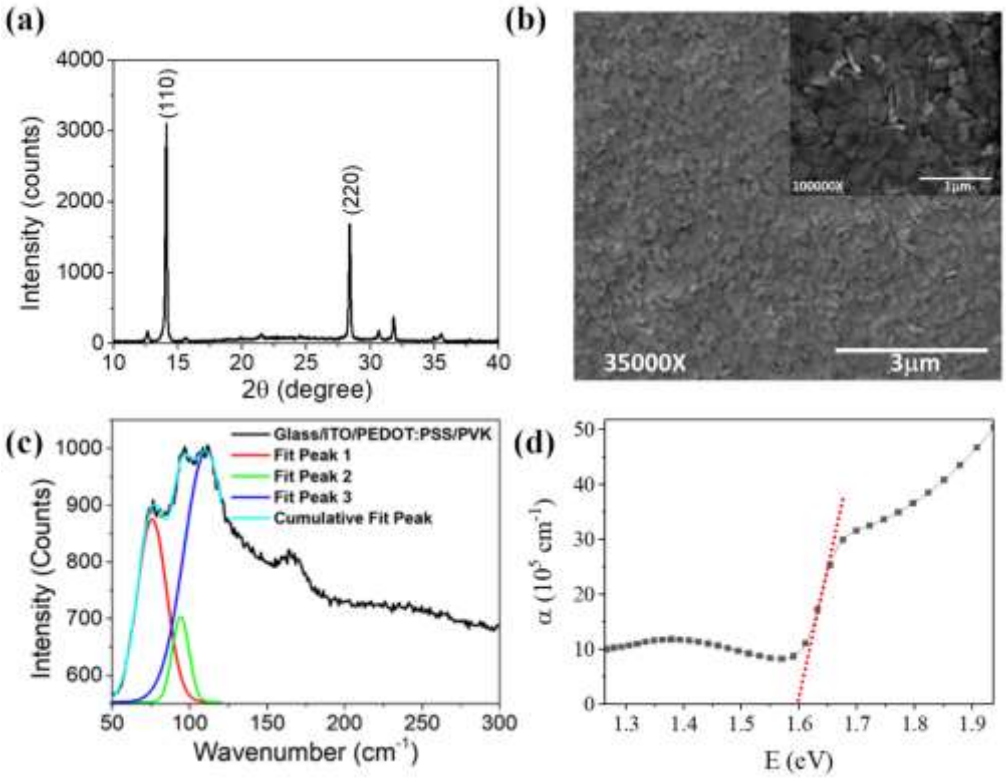

Figure 3

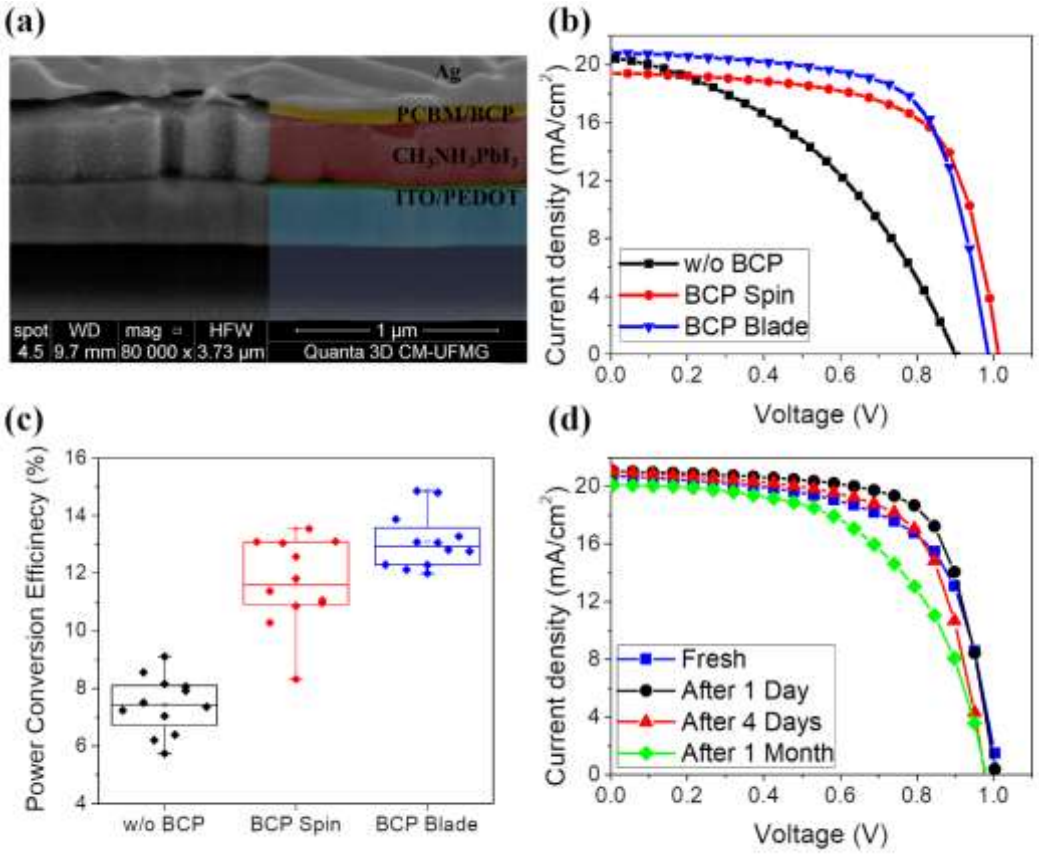

Figure 4

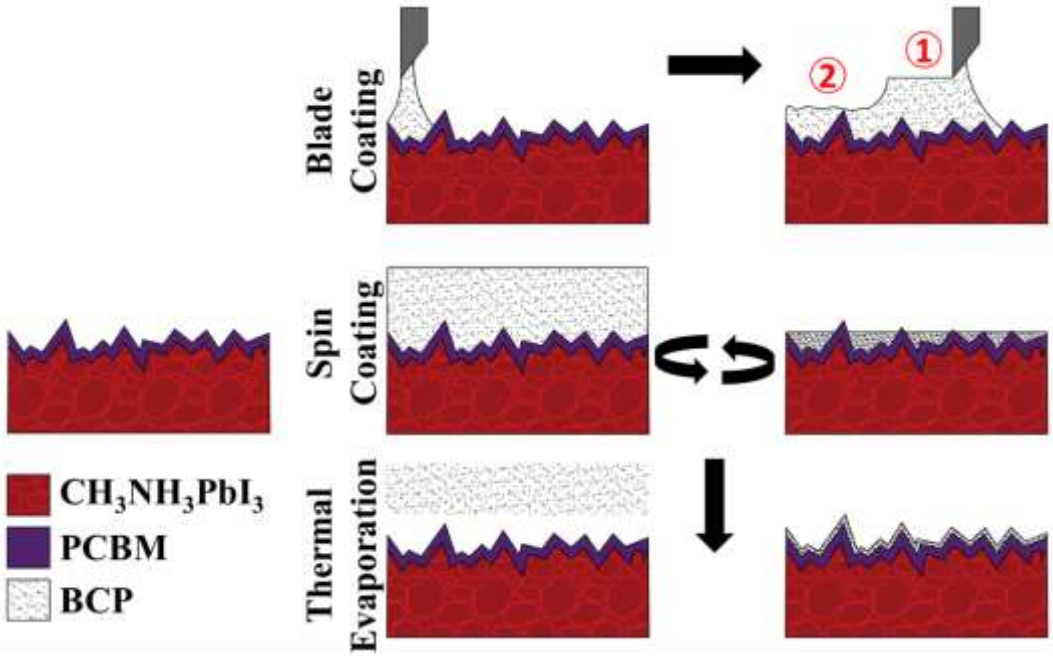

Figure 5

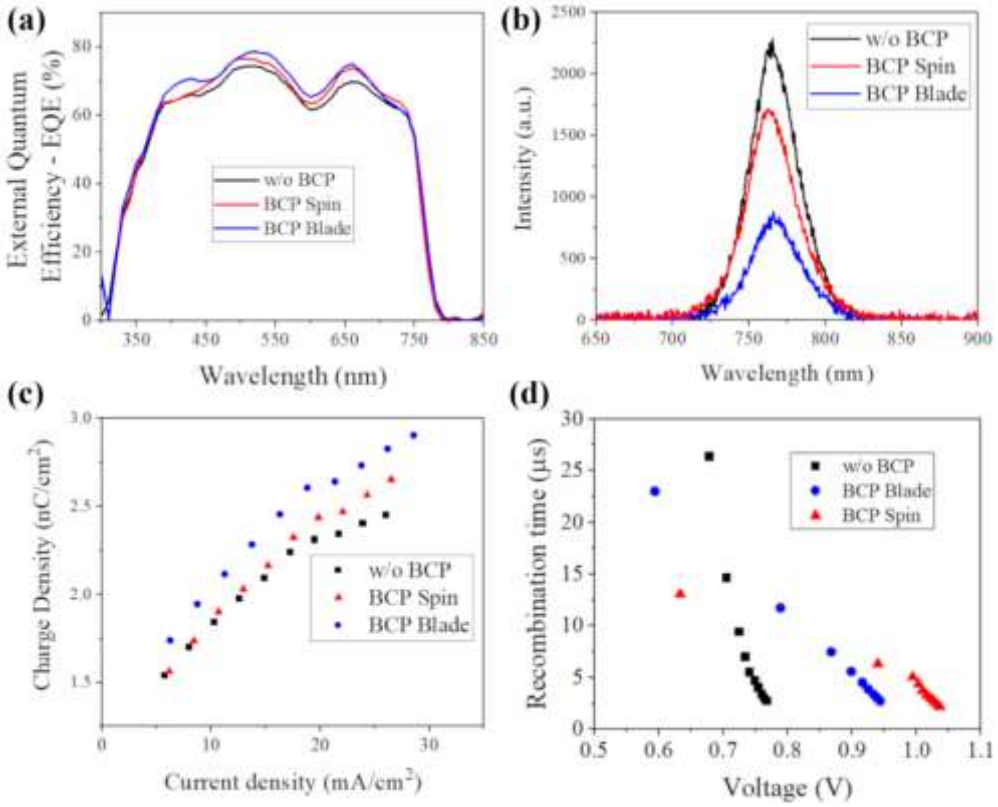

Figure 6

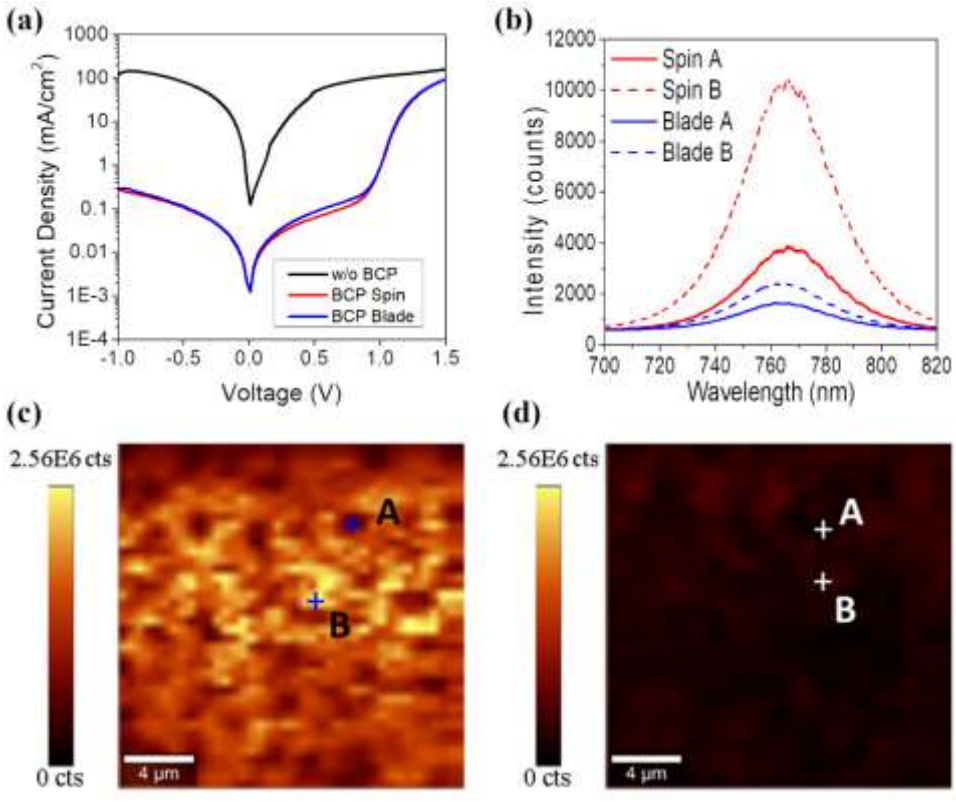

Figure 7

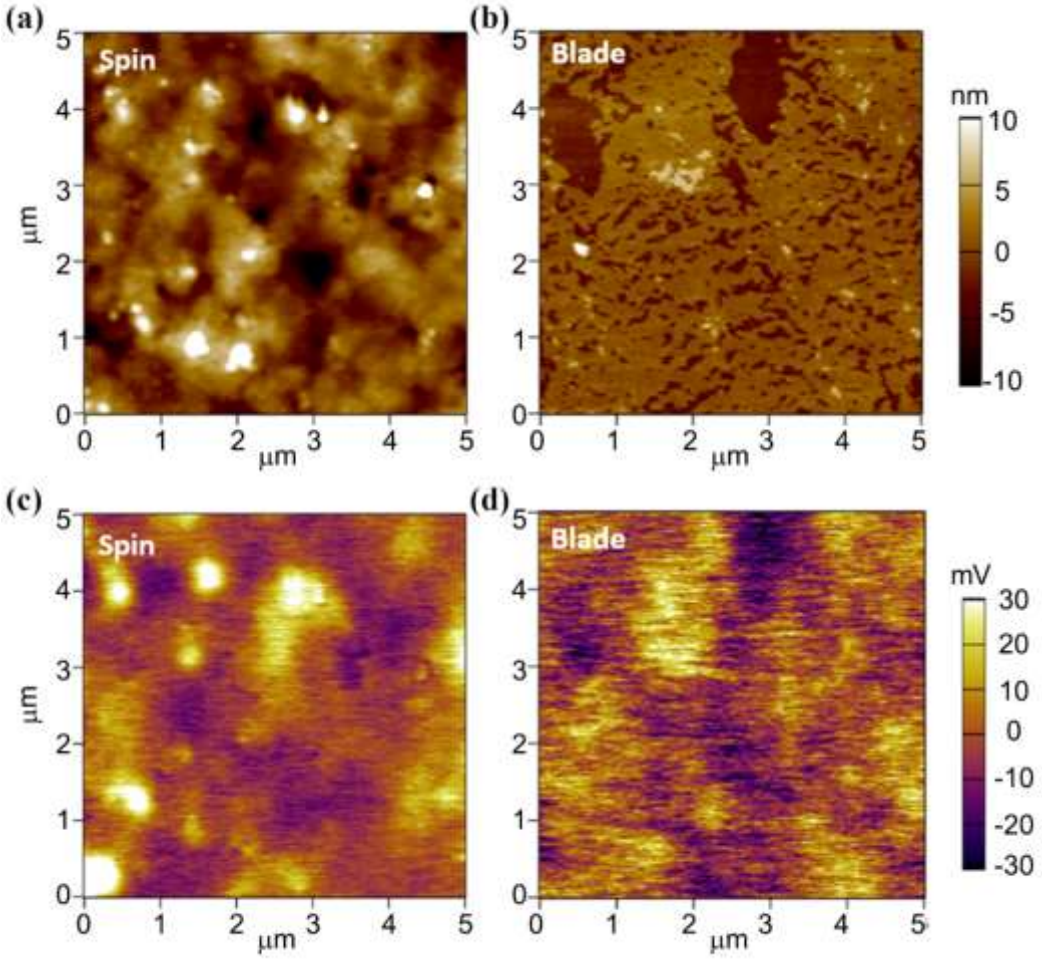
(a)
Spin
(b)
Blade
nm
10
5
0
-5
-10
(c)
Spin
(d)
Blade
mV
30
20
10
0
-10
-20
-30
µm
0
1
2
3
4
5